Experimental observation of the origin and structure of elastoinertial turbulence

George H. Choueiri[a,b], Jose M. Lopez[a,c], Atul Varshney[a], Sarath Sankar[a], and Björn Hof[a,1]

[a]Institute of Science and Technology, 3400 Klosterneuburg, Austria; [b]Mechanical, Industrial and Manufacturing Engineering (MIME) Department, University of Toledo, Toledo, OH 43606; and [c]Physics Department, Universitat Politècnica de Catalunya, 08034 Barcelona, Spain

Edited by H. K. Moffatt, University of Cambridge, Cambridge, United Kingdom, and approved October 6, 2021 (received for review February 4, 2021)

Turbulence generally arises in shear flows if velocities and hence, inertial forces are sufficiently large. In striking contrast, viscoelastic fluids can exhibit disordered motion even at vanishing inertia. Intermediate between these cases, a state of chaotic motion, "elastoinertial turbulence" (EIT), has been observed in a narrow Reynolds number interval. We here determine the origin of EIT in experiments and show that characteristic EIT structures can be detected across an unexpectedly wide range of parameters. Close to onset, a pattern of chevron-shaped streaks emerges in qualitative agreement with linear and weakly nonlinear theory. However, in experiments, the dynamics remain weakly chaotic, and the instability can be traced to far lower Reynolds numbers than permitted by theory. For increasing inertia, the flow undergoes a transformation to a wall mode composed of inclined near-wall streaks and shear layers. This mode persists to what is known as the "maximum drag reduction limit," and overall EIT is found to dominate viscoelastic flows across more than three orders of magnitude in Reynolds number.

elastoinertial turbulence | viscoelastic flows | elastic instability | drag reduction

Many fluids in nature and applications, such as paints, polymer melts, or saliva, have viscous as well as elastic properties, and their flow dynamics fundamentally differ from that of Newtonian fluids. A standard example of such viscoelastic fluids is solutions of long-chain polymers, and here, surprisingly even very dilute solutions show a drastic suppression of turbulence and significantly lower drag levels (1, 2), a phenomenon commonly exploited in pipeline flows to save pumping costs. In seeming contradiction to this stabilizing effect are observations at much lower Reynolds numbers (Re; the ratio of inertial to viscous forces), where polymers have the exact opposite effect; they initiate fluctuations and increase the flow's drag. The resulting chaotic motion was first detected in a narrow Reynolds number interval, $1{,}000 \lessapprox Re \lessapprox 2{,}000$, just below the onset of ordinary turbulence (3, 4) and interpreted as a form of early turbulence. However, it was later shown (5) that the corresponding elastoinertial instability can be traced to the polymer drag reduction regime at larger Re. The suggestion of a possible connection between these two seemingly opposing effects has sparked much recent interest in the phenomenon of elastoinertial turbulence (EIT) (6–13).

It has additionally been speculated that EIT may be connected to purely "elastic turbulence," a fluctuating state driven by a linear elastic instability in the inertialess limit (14). This instability requires curved streamlines (14–16) and is hence not to be expected in flows through smooth straight pipes. This does not, however, rule out the possibility that in planar flows, the instability may arise nonlinearly (17), and this possibility has been supported by recent experiments (18, 19).

Although EIT was first observed in pipe flow experiments (3, 4), information on the structure and nature of the resulting state is almost exclusively based on simulations using polymer models. Such simulations and theoretical considerations have suggested a range of possible transition scenarios. In direct numerical simulations (employing the Finitely Extensible Nonlinear Elastic-Peterlin [FENE-P] model), the characteristic features of EIT include near-wall vortical structures oriented perpendicular to the mean flow direction (i.e., spanwise direction) and elongated sheets of constant polymer stretch inclined with respect to the wall. In these simulations, the transition leading to this state is nonlinear (i.e., subcritical) and requires perturbations of finite amplitude (5–7). In another study, the aforementioned spanwise vortical structures were suggested to be linked to the well-known Tollmien–Schlichting (TS) instability that occurs in channel flow of Newtonian fluids at substantially larger Reynolds numbers. Again, here the transition would be subcritical but linked to TS waves (8). Yet other studies reported a linear instability that gives rise to chevron-shaped streaks (9). The latter proposed that this supercritical transition may be the starting point of a sequence of instabilities that eventually lead to EIT. Even more recently, FENE-P simulations of a simplified two-dimensional (2D) variant of EIT identified a subcritical scenario linked to the aforementioned linearly unstable mode (12).

In the present study, we visualize the onset of EIT in experiments and show that the flow pattern is in excellent agreement with the unstable mode predicted by linear stability analysis (9). However, in experiments, fluctuations are already present close to onset, suggesting that nonlinear effects cannot be neglected. Moreover, for increasing elasticity number, the instability can be pushed to Re an order of magnitude below the parameter regime predicted by linear analysis. Although a quantitative comparison between experiments and computations remains challenging due to model limitations and difficulties in characterizing fluids,

Significance

The motion of viscoelastic fluids often strikingly differs from the Newtonian standard case. Elastic fluid properties tend to give rise to instability and chaotic motion at low inertia yet suppress turbulence at high inertia. In experiments of polymer solutions, we identify the dynamical mode that dominates the onset of the recently discovered state of "elastoinertial turbulence" (EIT), and our observations allow us to discriminate between the various theoretical models attempting to explain the state's origin. Moreover, we demonstrate that the characteristic EIT structures can be traced across more than three orders of magnitude in Reynolds number, suggesting that EIT plays as dominant a role in high-shear viscoelastic flows as ordinary turbulence does in high-inertia Newtonian flows.

Author contributions: G.H.C., J.M.L., and B.H. designed research; G.H.C., J.M.L., A.V., and S.S. performed research; G.H.C., J.M.L., A.V., and S.S. analyzed data; and G.H.C., J.M.L., A.V., and B.H. wrote the paper.

The authors declare no competing interest.

This article is a PNAS Direct Submission.

[1]To whom correspondence may be addressed. Email: bhof@ist.ac.at.

This article contains supporting information online at https://www.pnas.org/lookup/suppl/doi:10.1073/pnas.2102350118/-/DCSupplemental.

Published November 3, 2021.

overall these observations suggest that the instability scenario is subcritical, an aspect that is also in line with the recent model study of EIT limited to two dimensions (12). For increasing *Re* on the other hand, the dominant flow structures adjust from a center to a wall mode, and fluctuation levels strongly increase. The resulting three-dimensional EIT flow pattern persists to the so-called "maximum drag reduction" (MDR) regime at much larger *Re*. Structural features of EIT can hence be detected across more than three decades in *Re*.

Results

Experiments were initially performed using a 50% water glycerol mixture as solvent and dissolving 600 parts per million (ppm) polyacrylamide with a molecular weight of 5×10^6 Da (PAAm). The viscosity ratio (solvent/solution) of the fluid is $\beta = 0.5$, while the elasticity number $E = 8\lambda\nu/D^2 = 3.4$ (where λ is the fluid's relaxation time, ν is its kinematic viscosity, and D is the pipe diameter). The SD of the pressure fluctuations recorded for increasing Reynolds numbers is plotted in Fig. 1*A*. The fluctuation level is initially zero (when subtracting the sensor's background noise level), meaning that the flow is laminar, but it begins to grow at $Re \approx 18$ as the elastoinertial instability sets in. After the onset of instability, the fluctuation amplitude grows continuously with increasing *Re*, approximately in proportion to the square root of *Re* as indicated by the solid line. Nevertheless, given the small amplitudes and experimental uncertainties, other scaling relations cannot be ruled out.

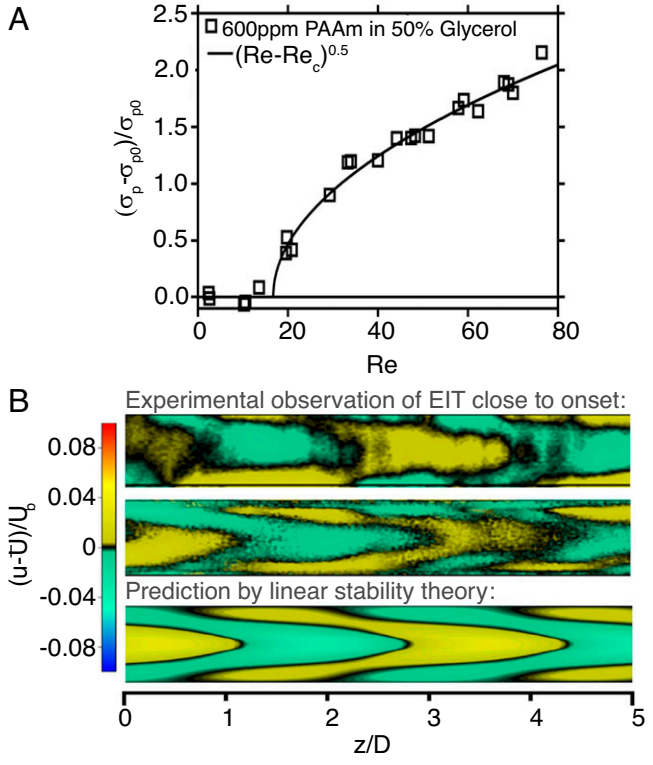

Fig. 1. Fluctuations level and flow structure near the onset of elastoinertial instability. (*A*) Evolution of the pressure fluctuations amplitude with increasing *Re* close to the instability threshold for experiments using 600 ppm of PAAm dissolved in a 50% water glycerol mixture. The symbol σ_p denotes the SD of the pressure fluctuations, $\sqrt{< p^2 >}$, whereas σ_{p_0} indicates the SD of the background noise level for the pressure sensor, $\sqrt{< p_0^2 >}$. (*B*) Flow structures composition at Reynolds numbers near transition. *Top* and *Middle* show streamwise velocity fluctuations obtained from PIV measurements in a longitudinal cross-section. *Top* shows flow structures at $Re \approx 5$ and corresponds to an experiment using a 66% glycerol concentration ($\beta = 0.57$, $E = 20.8$, $W_i = 104$), whereas *Middle* corresponds to $Re \approx 100$ in an experiment using a 50% glycerol concentration ($\beta = 0.5$, $E = 3.4$, $W_i = 304$). *Lower* shows the most unstable mode in the linear stability analysis; the solution plotted is intended for qualitative comparison only and was computed for different flow parameters: $Re = 100$, $E = 0.6$, $W_i = 60$, $\beta = 0.9$, $n = 0$, and $k = 1$; here, *n* and *k* are the azimuthal and axial wave numbers, respectively. Flow direction is from right to left.

Structural information is obtained from the velocity fields recorded in the pipe's central plane using particle image velocimetry (PIV). The instantaneous snapshots are assembled by applying Taylor's frozen-flow hypothesis, and the resulting flow structure is shown in Fig. 1*B*, *Middle* for $Re \approx 100$. For visualization purposes, the average cross-sectional velocity profile $\bar{U}$ is subtracted from the data, and areas with velocities lower (higher) than the mean profile are shown in green (yellow). These low- and high-speed streaks alternate in the streamwise direction and show a tendency to form a chevron-type pattern. To compare these flow patterns with the unstable mode predicted by the linear stability theory, we repeated the analysis in ref. 9. The obtained results are in excellent agreement with those in ref. 9. The least stable mode for $Re = 100$ is shown in Fig. 1*B*, *Bottom*. As seen, here, a chevron-type pattern consisting of alternating low- and high-speed streaks is also observed. Hence, the least stable mode can be detected in experiments, suggesting that the elastoinertial instability mechanism described in ref. 9 is indeed central to the onset of EIT. However, while the stability analysis predicts a perfectly regular structure (resulting from a supercritical Hopf bifurcation), in our case the structure is not singly periodic, but fluctuations appear across a range of frequencies, suggesting weakly chaotic flow. Attempts to resolve the flow field closer to onset of instability for the same fluid were unsuccessful due to the vanishing fluctuation amplitude and lower signal to noise ratio. As the onset of EIT is approached, the fluctuation levels approach zero continuously. This is in contrast to Newtonian turbulence, where the internal dynamics of puffs have far larger amplitudes.

In order to probe if the elastoinertial instability persists to even lower *Re*, additional experiments were carried out for a 66% glycerol water solution, again adding 600 ppm of PAAm. The more viscous solution has a six times larger elasticity number ($E = 20.8, \beta = 0.57$). Indeed, for the 66% glycerol water mixture, fluctuations were detected at *Re* as low as 5, whereas at slightly lower $Re \sim 3$, the flow was laminar. As shown in Fig. 1*B*, *Top*, at $Re = 5$, the flow again consists of alternating high- and low-speed streaks arranged in a chevron pattern. It is noteworthy that according to the linear analysis (9), the instability can only be continued to $Re \sim 80$ or so; this, however, does not rule out the possibility that the same mode may occur subcritically at even lower *Re*. Moreover, the flow pattern observed in our experiments at $Re = 5$ is again not perfectly periodic (unlike predicted by linear theory) but still weakly chaotic. Both these observations are consistent with a subcritical scenario where the minimum-amplitude threshold to trigger the instability, albeit finite, is low compared with the disturbance levels induced by typical experimental imperfections. In such a situation, EIT would arise automatically, even though in principle, the laminar state is linearly stable. The irregularities of the flow pattern observed are an indication that the state has undergone further bifurcations, and the resulting flow is chaotic and three-dimensional in nature.

We next investigate the further development of the flow pattern with increasing inertia (higher *Re*). In order to reach larger *Re*, the solvent was changed to water, again dissolving 600 ppm of PAAm and resulting in an elasticity number $E = 0.08$. Owing to the reduced elasticity number, the onset of instability shifts to larger *Re* (> 200). Also, for the 600-ppm PAAm solution in water, the transition appears to be continuous (Fig. 2*A*, *Inset*). With increasing *Re*, the fluctuation level does not saturate but instead, begins to increase faster; subsequently, the scaling

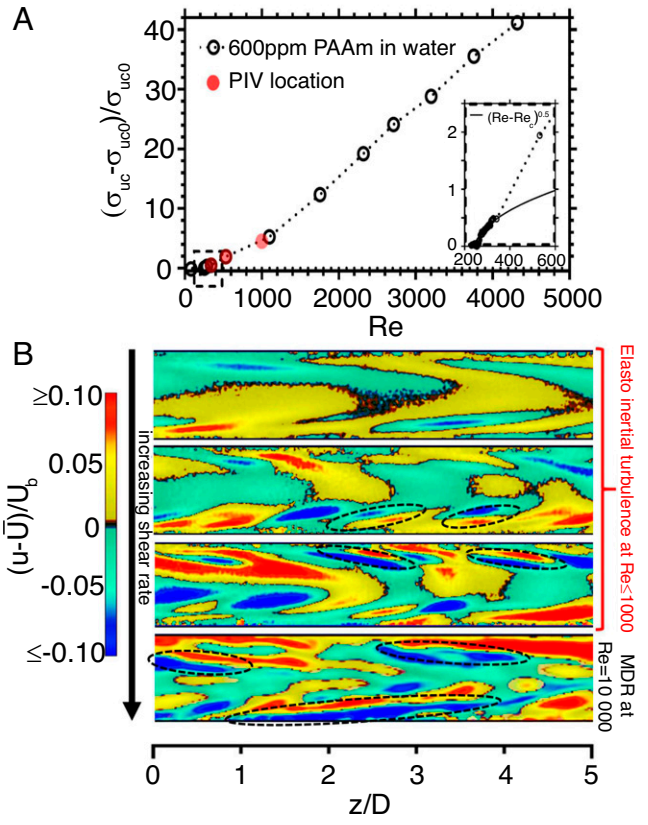

Fig. 2. Flow development far from the instability onset. (*A*) Variation of the streamwise velocity fluctuations at the pipe center with increasing *Re* in experiments using 600 ppm of PAAm dissolved in water. The symbols σ_{u_c} and $\sigma_{u_{co}}$ denote the SD of streamwise velocity fluctuations at the pipe centerline, $\sqrt{< u_c^2 >}$, and the SD of the background noise level for the LDV system, $\sqrt{< u_{co}^2 >}$, respectively. *Inset* shows the deviation from the square root scaling. The red dots indicate the locations where the flow structures shown in *B* were measured. (*B*) PIV visualizations of streamwise velocity fluctuations. From top to bottom, $Re = 300$, $Re = 500$, $Re = 1{,}000$, and $Re = 10{,}000$. With increasing shear, large-amplitude streaks (red, blue) arise in the near-wall region. Streaks become more elongated with *Re* and are separated by inclined shear layers (indicated by the dashed contours).

becomes closer to linear (Fig. 2*A*). At the lowest *Re* (= 300) where PIV measurements were carried out, the flow pattern still bears some resemblance to the chevron pattern (yellow and green isolevels shown in the first panel of Fig. 2*B*); however, in the near-wall region, higher-amplitude streaks (red and blue isolevels) have appeared. While for the chevron patterns (Fig. 1*B*), fluctuation profiles show a central peak, the appearance of the large-amplitude streaks qualitatively alters the flow pattern to a wall mode as shown in Fig. 2*B*. With a further increase in *Re*, the near-wall streaks continue to increase in amplitude, while the chevron mode in the central region of the pipe disappears (the second panel in Fig. 2*B*). Inclined near-wall structures [often visualized in terms of polymer stretch (5, 6)] are a characteristic feature of EIT in numerical simulations; however, to date, inclined structures could not be confirmed in experiments.

Note that this mode change is equally found in the higher-viscosity solvents (50 and 66% glycerol concentrations) for *Re* sufficiently larger than those shown in Fig. 1*B*. With increasing shear levels, low- and high-speed streaks often appear in pairs that are approximately parallel, signifying strong shear layers at the respective interface (dashed black contours in Fig. 2*B*). Shear layers just like streaks are inclined with respect to the main flow direction and become more elongated with increasing *Re*, often extending multiple pipe diameters. We speculate that this mode change may result from a secondary instability. The generation of streak pairs has also been observed in a numerical study, albeit in the absence of walls, in homogeneous viscoelastic shear flow (20). As *Re* is further increased to $Re = 1{,}000$ (the third panel in Fig. 2*B*), there is surprisingly little change in the overall flow structure, and the wall mode continues to dominate the dynamics. Even for a 10-fold increase to $Re = 10{,}000$ (the fourth panel in Fig. 2*B*) and hence, a value that is well into the classical polymer drag reduction regime, the wall mode persists, and the flow's structural composition closely resembles that of EIT at $Re = 1{,}000$, while it is clearly distinct from Newtonian turbulence (Fig. 3, *Inset*).

In addition to velocity measurements, the pressure drop was recorded as $Re = 10,000$ was approached in order to determine fluid drag. The corresponding friction factors relative to the laminar level are shown in Fig. 3. At low Reynolds numbers, friction factors of EIT (red points) only marginally exceed the laminar friction. With increasing *Re*, deviations become notable, and the friction values smoothly approach what is known as the MDR or Virk's asymptote (red line). Regardless of the type of polymer, solvent, and relative concentration, Virk's asymptote sets a universal limit to the amount of drag reduction obtainable. Traditionally, MDR has been proposed as a residual, minimal level of ordinary turbulence, and a relation to the edge state of Newtonian turbulence has been suggested (1, 2, 21, 22). This interpretation does not readily explain why polymers cannot reduce the drag beyond this level [reduction beyond MDR can be achieved in a narrow parameter regime only (10) but not at high *Re*]. As first suggested in ref. 5, the MDR scaling may instead be caused by the EIT instability (i.e., although polymers can largely suppress ordinary Newtonian-type turbulence, eventually when shear levels are sufficiently large, the elastoinertial instability necessarily must arise, inhibiting laminarization).

It is noteworthy that in the present study as the high-inertia regime is approached, the MDR friction scaling monotonically arises from low Reynolds number EIT. Structurally, MDR and EIT are equally composed of elongated inclined streaks and shear layers. In contrast, streaks in Newtonian turbulence are shorter and less coherent (Fig. 3). In addition to the structural composition and the skin friction levels, the Reynolds shear stress also (Fig. 3, *Inset*) smoothly links low–Reynolds number EIT and high–Reynolds number MDR, whereas Newtonian turbulence levels are an order of magnitude larger (23). The same

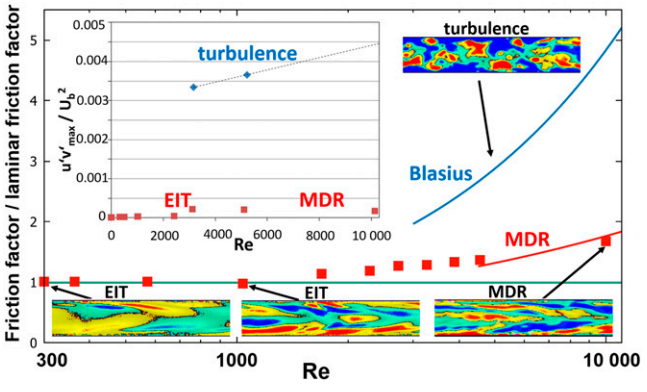

Fig. 3. Evolution of friction factors with increasing *Re*. At low *Re*, the friction factors of EIT (red points) are indistinguishable from the laminar friction values (green line). With increasing *Re*, the friction factors visibly exceed the laminar level and continuously approach the MDR asymptote (red curve). *Inset* shows Reynolds stresses normalized by the square of the bulk flow velocity for Newtonian turbulence. EIT and MDR are at the same level, whereas turbulent Reynolds stresses are an order of magnitude larger.

holds for velocity fluctuations (Fig. 2*A*). It should be taken into account that unlike EIT, Newtonian turbulence necessarily arises via spatially localized structures (puffs and slugs) and spatiotemporal intermittency. These localized structures require finite-amplitude fluctuation and friction levels and hence, do not smoothly develop from low levels. EIT, on the other hand, is never spatially localized but always space filling, a feature that persists during its development to high *Re* and MDR.

The state space considered in this work, although broad in terms of Reynolds and elasticity numbers, represents only a subset of possible parameters. For example, the dependence on polymer concentration, Weissenberg number, viscosity ratio, polymer chain length, etc. have not been explored and are left for future studies. In particular, it will be interesting to explore if in a different part of parameter space, the chevron pattern at onset may settle to the exact axisymmetric (i.e., 2D) chevron mode, as predicted by linear analysis.

In summary, we have shown in experiments that EIT arises from a center mode chevron pattern in qualitative agreement with linear stability theory (9). From theoretical considerations, it is evident that this mode requires finite inertia (9). This relevance of inertia suggests that EIT is distinct from purely elastic turbulence, although a more recent theoretical study (24) indicates a connection between the two instability mechanisms at least for a very narrow parameter window. On the other hand, the transition is considerably more complex than the instability suggested by linear analysis (9). Although fluctuation amplitudes appear to increase continuously and at first sight seem to support a linear instability and a supercritical scenario, as shown in Fig. 4*A* the onset of EIT can be pushed to Reynolds numbers more than an order of magnitude lower than permitted by the linear theory. Moreover, linear theory predicts a nonmonotonic dependence of the critical Reynolds number at which the instability occurs; in experiments, we find that the threshold decreases monotonically. Although given the difficulties in modeling and characterizing polymer solutions, a quantitative comparison between experiments and theory remains challenging, the monotonic decrease to very low Reynolds numbers strongly supports a subcritical scenario. This subcritical nature is equally supported by the chaotic three-dimensional motion detected even close to onset. On the other hand, experiments cannot strictly rule out that upon an even closer approach to the critical point, the flow pattern may yet settle to the unperturbed (supercritical) mode.

In order to allow quantitative comparison with experiments, future theories must take nonlinear effects and the three-dimensional nature of EIT in experiments into account. Regarding the latter, shortcomings of 2D simulations have also been pointed out in a recent numerical study (25). With respect to the former, a theoretical (Riemannian) framework enabling a (weakly) nonlinear approach has been introduced recently (26, 27). Subsequent to the present study, weakly nonlinear analyses have been carried out for pipe (28) and channel (29) flows and established the robustness of the chevron mode (figure 8A in ref. 28). These findings retrospectively rationalize the mode's persistence to the weakly chaotic regime reported in the present experiments. Moreover, both theoretical studies tested our suggestion that a subcritical route may not be readily distinguishable from a supercritical one under realistic experimental conditions if threshold amplitudes, albeit finite, remain small. As shown by ref. 29, even well into the subcritical regime, threshold amplitude indeed remains small. Looking beyond the regime traceable by stability analysis, our experimental observations suggest that nonlinear effects are in particular relevant for the flow's subsequent transformation from a center (Fig. 4*B*, red points) to a wall mode (blue points). It is this latter flow transition that gives rise to the near-wall inclined structures characteristic for EIT (5) and to a more rapid increase of fluctuation levels. This structural change occurs at *Re* of order 10^2 and hence, far below the inertia levels required for Newtonian-type turbulence. The resulting flow pattern remains qualitatively unchanged with increasing *Re*, demonstrating that EIT is active in the MDR limit and hence, inhibits flow laminarization even if polymers ultimately were to completely eradicate ordinary turbulence.

Materials and Methods

Methods. Experiments are carried out in a 1.1-m-long smooth glass pipe with an inner diameter $D = 4$ mm. A smooth inlet ensures that the gravity-driven water flow remains laminar to *Re* greater than 5,000. Starting from 150*D* downstream of the inlet, the pressure drop is measured over a pipe length of 75*D* using a differential pressure sensor (DP15; Validyne Engineering). Directly downstream, an identical sensor is used to measure pressure fluctuations over a pipe length of 4*D*. A planar PIV system (LaVision GmbH), located 250*D* downstream of the pipe inlet, is employed to monitor the velocity field in a radial–axial cross-section. At the same location and positioned at the pipe center, a laser Doppler velocimetry (LDV) system (Powersight; TSI GmbH) is used to measure the axial velocity component.

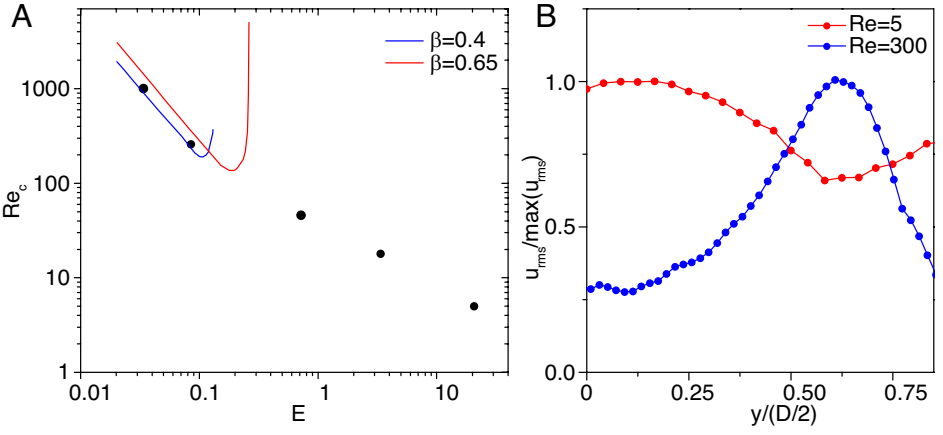

Fig. 4. Onset of EIT. (*A*) Elasticity number dependence of the transition threshold. In experiments (black circles), the transition Reynolds number for the onset of EIT decreases monotonically with the elasticity number. While at low elasticity numbers, the experimental data are in good agreement with the threshold predicted by linear stability theory (9), linear analysis predicts a nonmonotonic dependence that is not found in experiments. At high elasticity numbers, the onset of EIT occurs at *Re* more than an order of magnitude below the theoretical prediction. (*B*) Change from a center to a wall mode with increasing *Re*. For the chevron pattern EIT exhibits close to onset (Fig. 1*A*), the rms of the streamwise velocity fluctuations has a peak close to the pipe center (red data points, $Re = 5$, $E = 20.8$). Sufficiently far above onset, the central peak disappears, and the highest fluctuations are found closer to the wall (i.e., at the location of the inclined streaks and shear layers [the second panel in Fig. 2*B*]; $Re = 300$, $E = 0.08$).

The working fluid is a 600-ppm (by weight) PAAm (lot 685910; Polysciences, Inc.) solution in either water or water glycerol mixtures (50 and 66% glycerol). The addition of glycerol effectively increases the viscosity of the Newtonian solvent and allows us to investigate flows at low Reynolds numbers while keeping the shear rates and hence, elastic forces (or more precisely, the Weissenberg number) high. The chosen polymer concentration approaches the upper end of the dilute limit (estimated from the measure of intrinsic viscosity to be $\approx$ 700 ppm).

Data Availability. All study data are included in the article and/or *SI Appendix*.

ACKNOWLEDGMENTS. We thank Y. Dubief, R. Kerswell, E. Marensi, V. Shankar, V. Steinberg, and V. Terrapon for discussions and helpful comments. A.V. and B.H. acknowledge funding from the Austrian Science Fund, grant I4188-N30, within the Deutsche Forschungsgemeinschaft research unit FOR 2688.

1. I. Procaccia, V. S. L'vov, R. Benzi, Colloquium: Theory of drag reduction by polymers in wall-bounded turbulence. *Rev. Mod. Phys.* **80**, 225–247 (2008).
2. C. M. White, M. G. Mungal, Mechanics and prediction of turbulent drag reduction with polymer additives. *Annu. Rev. Fluid Mech.* **40**, 235–256 (2008).
3. A. Ram, A. Tamir, Structural turbulence in polymer solutions. *J. Appl. Polym. Sci.* **8**, 2751–2762 (1964).
4. R. C. Little, M. Wiegard, Drag reduction and structural turbulence in flowing polyox solutions. *J. Appl. Polym. Sci.* **14**, 409–419 (1970).
5. D. Samanta *et al.*, Elasto-inertial turbulence. *Proc. Natl. Acad. Sci. U.S.A.* **110**, 10557–10562 (2013).
6. Y. Dubief, V. E. Terrapon, J. Soria, On the mechanism of elasto-inertial turbulence. *Phys Fluids (1994)* **25**, 110817 (2013).
7. J. M. Lopez, G. H. Choueiri, B. Hof, Dynamics of viscoelastic pipe flow at low reynolds numbers in the maximum drag reduction limit. *J. Fluid Mech.* **874**, 699–719 (2019).
8. A. Shekar, R. M. McMullen, S. N. Wang, B. J. McKeon, M. D. Graham, Critical-layer structures and mechanisms in elastoinertial turbulence. *Phys. Rev. Lett.* **122**, 124503 (2019).
9. P. Garg, I. Chaudhary, M. Khalid, V. Shankar, G. Subramanian, Viscoelastic pipe flow is linearly unstable. *Phys. Rev. Lett.* **121**, 024502 (2018).
10. G. H. Choueiri, J. M. Lopez, B. Hof, Exceeding the asymptotic limit of polymer drag reduction. *Phys. Rev. Lett.* **120**, 124501 (2018).
11. B. Chandra, V. Shankar, D. Das, Onset of transition in the flow of polymer solutions through microtubes. *J. Fluid Mech.* **844**, 1052–1083 (2018).
12. J. Page, Y. Dubief, R. R. Kerswell, Exact traveling wave solutions in viscoelastic channel flow. *Phys. Rev. Lett.* **125**, 154501 (2020).
13. B. Chandra, V. Shankar, D. Das, Early transition, relaminarization and drag reduction in the flow of polymer solutions through microtubes. *J. Fluid Mech.* **885**, A47 (2020).
14. A. Groisman, V. Steinberg, Elastic turbulence in a polymer solution flow. *Nature* **405**, 53–55 (2000).
15. R. G. Larson, E. S. G. Shaqfeh, S. J. Muller, A purely elastic instability in Taylor–Couette flow. *J. Fluid Mech.* **218**, 573–600 (1990).
16. E. S. Shaqfeh, Purely elastic instabilities in viscometric flows. *Annu. Rev. Fluid Mech.* **28**, 129–185 (1996).
17. A. N. Morozov, W. van Saarloos, Subcritical finite-amplitude solutions for plane Couette flow of viscoelastic fluids. *Phys. Rev. Lett.* **95**, 024501 (2005).
18. L. Pan, A. Morozov, C. Wagner, P. E. Arratia, Nonlinear elastic instability in channel flows at low Reynolds numbers. *Phys. Rev. Lett.* **110**, 174502 (2013).
19. B. Qin, P. F. Salipante, S. D. Hudson, P. E. Arratia, Flow resistance and structures in viscoelastic channel flows at low re. *Phys. Rev. Lett.* **123**, 194501 (2019).
20. J. Page, T. A. Zaki, The dynamics of spanwise vorticity perturbations in homogeneous viscoelastic shear flow. *J. Fluid Mech.* **777**, 327–363 (2015).
21. L. Xi, M. D. Graham, Active and hibernating turbulence in minimal channel flow of Newtonian and polymeric fluids. *Phys. Rev. Lett.* **104**, 218301 (2010).
22. L. Xi, M. D. Graham, Dynamics on the laminar-turbulent boundary and the origin of the maximum drag reduction asymptote. *Phys. Rev. Lett.* **108**, 028301 (2012).
23. M. D. Warholic, H. Massah, T. J. Hanratty, Influence of drag-reducing polymers on turbulence: Effects of Reynolds number, concentration and mixing. *Exp. Fluids* **27**, 461–472 (1999).
24. M. Khalid, V. Shankar, G. Subramanian, A continuous pathway between the elasto-inertial and elastic turbulent states in viscoelastic channel flow. *Phys. Rev. Lett.* **127**, 134502 (2021).
25. L. Zhu, L. Xi, Inertia-driven and elastoinertial viscoelastic turbulent channel flow simulated with a hybrid pseudo-spectral/finite-difference numerical scheme. *J. Non-Newt. Fluid Mech.* **286**, 104410 (2020).
26. I. Hameduddin, C. Meneveau, T. A. Zaki, D. F. Gayme, Geometric decomposition of the conformation tensor in viscoelastic turbulence. *J. Fluid Mech.* **842**, 395–427 (2018).
27. I. Hameduddin, D. F. Gayme, T. A. Zaki, Perturbative expansions of the conformation tensor in viscoelastic flows. *J. Fluid Mech.* **858**, 377–406 (2019).
28. D. Wan, G. Sun, M. Zhang, Subcritical and supercritical bifurcations in axisymmetric viscoelastic pipe flows. arXiv [Preprint] (2021). https://arxiv.org/abs/2108.00220 (Accessed 21 August 2021).
29. G. Buza, J. Page, R. R. Kerswell, Weakly nonlinear analysis of the viscoelastic instability in channel flow for finite and vanishing Reynolds numbers. arXiv [Preprint] (2021). https://arxiv.org/abs/2107.06191 (Accessed 21 August 2021).